Available online at www.sciencedirect.com

SCIENCE DIRECT®

Journal of Solid State Chemistry 179 (2006) 70–76

JOURNAL OF SOLID STATE CHEMISTRY

www.elsevier.com/locate/jssc

Structure and magnetism of 4H-BaMnO$_{3-x}$ ($0 \leqslant x \leqslant 0.35$) and 4H-Ba$_{0.5}Sr_{0.5}MnO_{3-x}$ ($0 \leqslant x \leqslant 0.21$)

Josephine J. Adkin, Michael A. Hayward*

Department of Chemistry, Inorganic Chemistry Laboratory, University of Oxford, South Parks Road, Oxford, OX1 3QR, UK

Received 15 August 2005; received in revised form 16 September 2005; accepted 24 September 2005
Available online 2 November 2005

Abstract

The synthesis and structure determination of 4H-BaMnO$_{3-x}$ ($0 \leqslant x \leqslant 0.35$) and 4H-Ba$_{0.5}Sr_{0.5}MnO_{3-x}$ ($0 \leqslant x \leqslant 0.21$) is described. Neutron powder diffraction data unambiguously show the anion vacancies in the oxygen-deficient phases lie in the hexagonal BaO$_{3-x}$ layers, rather than the cubic layers predicted by previous structural models. The localization of anion vacancies in the hexagonal layers is discussed on the basis of the local co-ordination polyhedra of the metal cations. Low-temperature neutron diffraction data show the oxidized materials adopt antiferromagnetic ordered structures (Ba$_{0.5}$Sr$_{0.5}$MnO$_{2.99}$: $T_N = 265\,K$). Anion-deficient phases do not achieve magnetic order suggesting the Mn(III/IV) charge disorder suppresses long-range magnetic order.

Keywords: Neutron diffraction; Hexagonal perovskite; Magnetic order

1. Introduction

In recent years there has been a continued interest in mixed-valent manganese (III)/(IV) oxides. This is largely due to the observation of large magnetoresistive ratios in phases with the AMnO$_3$ perovskite and A$_{n+1}$Mn$_n$O$_{3n-1}$ Ruddlesden–Popper structures [1–3]. These two structure types consist of arrays of apex-shared MnO$_6$ octahedra which are interspersed with AO rock-salt layers in the case of the layered Ruddlesden–Popper phases. The resulting Mn–O–Mn linkages have bond angles of approximately 180°, in the highest symmetry structures, through which magnetic exchange can occur. The structural tolerance factor, t ($t = \langle \text{A–O} \rangle / \sqrt{2} \langle \text{Mn–O} \rangle$) [4] can be used to measure the mismatch in the A–O and Mn–O bond lengths of AMnO$_3$ phases and thus predict the structure adopted by a particular composition. As the tolerance factor becomes smaller than the geometrically most desirable value of 1 for a cubic perovskite, increasingly distorted structures are adopted in which the Mn–O–Mn angle is reduced from 180° to accommodate small *A*-site cations. Considerable efforts have been made to try to understand the complex structure–property relationships of these distortions particularly when associated with variable mean manganese oxidation states [5,6]. A similar effort, however, has not been focused on phases containing large *A*-cations. If the tolerance factor takes values significantly greater than 1, hexagonal perovskite structures containing face-sharing MnO$_6$ octahedra are adopted [7]. The face-shared Mn–O–Mn linkages have bond angles of approximately 90°. This different geometry can lead to dramatic differences in super-exchange interactions compared with apex-shared connectivity [8]. The ratio of face-sharing to apex-sharing linkages in hexagonal perovskites is dependant on the size of the tolerance factor as demonstrated by the structural progression of the group-two AMnO$_3$ manganates. CaMnO$_3$ ($t = 0.987$) adopts a distorted cubic perovskite structure (all apex sharing) [9]; SrMnO$_3$ ($t = 1.033$) adopts a 4H structure (1:1 apex:face sharing) [10]; BaMnO$_3$ ($t = 1.089$) adopts a 2H structure (all face sharing) [11].

The average manganese oxidation state also influences the tolerance factor via an influence on the average manganese–oxygen bond length. Thus in the series of BaMnO$_{3-x}$ ($0 < x < 0.25$) phases, the ratio of apex to

---

*Corresponding author. Fax: +44 1865 272690.
E-mail address: michael.hayward@chem.ox.ac.uk (M.A. Hayward).

0022-4596/$ - see front matter © 2005 Elsevier Inc. All rights reserved.
doi:10.1016/j.jssc.2005.09.046

face-sharing linkages, or more specifically cubic to hexagonally stacked layers, changes smoothly with the non-stoichiometry, x, from 2H-$BaMnO_{3.00}$ to 4H-$BaMnO_{2.75}$ via a large number of intermediate compositions and structures [12]. However, this relationship restricts investigations which seek to independently probe structural and electronic influences on physical properties.

Recent work has shown it is possible to perform topotactic (structure conserving) redox reactions at low temperature on complex manganese oxide substrates [13]. This is achieved by performing reactions at low temperatures such that there is insufficient free energy to allow the structural rearrangement of the metal cations, but such that the more mobile oxide ions can be readily reductively deintercalated (or oxidatively intercalated) with the metal ions remaining essentially static. By applying this synthetic strategy to hexagonal manganates it should be possible to prepare metastable phases in which the average manganese oxidation state is decoupled from the crystal structure adopted by the material. As a preliminary to the topotactic reduction of $BaMnO_3$ phases we have investigated the anion vacancy distribution and oxidation chemistry of 4H-$BaMnO_{3-x}$ and 4H-$Ba_{0.5}Sr_{0.5}MnO_{3-x}$.

2. Experimental

6 g samples of 4H-$BaMnO_{3-x}$ and 4H-$Ba_{0.5}Sr_{0.5}MnO_{3-x}$ were prepared by a standard ceramic route. Suitable quantities of $BaCO_3$ (99.997%, Alfa Aesar), $SrCO_3$ (99.994%, Alfa Aesar) and MnO_2 (99.999%, Alfa Aesar) were thoroughly mixed in an agate pestle and mortar before being heated at 900 °C in air to decompose the carbonates. The resulting black powders were reground and pressed into 13 mm pellets at 5 tonne pressure before being heated for two periods of 2 days at 1300 °C under flowing argon. Samples were reground and pressed into pellets between heating periods. After the final heating period, samples were cooled at 10 °C/min to room temperature under argon. Thermogravimetric studies showed samples gained significant mass when heated at 600 °C under flowing oxygen, with no change in crystal symmetry as determined by X-ray powder diffraction. Therefore, bulk oxidized samples were prepared by heating 5 g samples under flowing oxygen at 600 °C for 6 h.

Neutron powder diffraction data suitable for structural refinement were collected from $BaMnO_{3-x}$ samples at room temperature using the HRPD diffractometer and at 5 K using the Polaris diffractometer at ISIS, UK. Neutron powder diffraction data were collected from $Ba_{0.5}Sr_{0.5}MnO_{3-x}$ samples using the D2B diffractometer at the ILL, Grenoble at room temperature and 5 K. Rietveld profile refinement was performed against diffraction data utilizing the GSAS suite of programs [14]. The average Mn oxidation state of phases was determined by dissolving samples in HCl containing an excess of KI and titrating the liberated I_2 with $Na_2S_2O_3$. Field-cooled and zero field-cooled magnetization data were collected as a function of temperature between 5 and 300 K. Field-cooled magnetization-field isotherms were collected between ±5 T using a Quantum Design MPMS SQUID magnetometer.

3. Results

3.1. Structural characterization

Powder diffraction data collected from all four samples could be readily indexed on the basis of the hexagonal cells detailed in Table 1, space group $P6_3/mmc$. Models based on the 4H stacking sequence, reported by Hardy [15] for $BaMnO_{3-x}$ and also observed for $SrMnO_3$ [10], were refined against neutron powder diffraction data. The atomic positions and anisotropic thermal parameters of all atoms were refined. In the case of mixed Ba/Sr phases, the relative fractions of Ba and Sr on the two A-cation sites were refined, under the constraint that the total Ba:Sr ratio remained unity, to allow A-site cation ordering. The occupancy fractions of the oxide ions in all samples were also refined. It was observed that the occupancy of the 6 g oxygen site in the Ba/Sr samples refined to values slightly greater than unity (~1.02). This site was therefore set and fixed at full occupancy in the structural models of these phases. Weak diffraction features corresponding to a small quantity (~1.4 mol%) of MnO were observed in data sets collected from unoxidized $BaMnO_{3-x}$ samples. Therefore, a second phase corresponding to MnO was added to the model refined against this data set. Results of the structural refinements and oxygen stoichiometries are given in Table 2, with selected bond lengths and angles in Table 3.

3.2. Magnetic characterization

It can be seen from the temperature-dependant magnetisation data collected from $BaMnO_{3-x}$ samples (Fig. 1) that in the temperature range $50 < T/K < 300$ the magnetisation of both samples decreases slowly with decreasing temperature. Both data sets show a sharp increase in magnetisation at $T \sim 50$ K accompanied by a divergence between the zero field-cooled and field-cooled data consistent with a magnetic transition on cooling below this temperature. Magnetisation-field isotherms collected from both samples at 300 K are linear and pass through the origin. However, field-cooled magnetisation-field isotherms collected at 5 K from both samples show magnetic hysteresis (Fig. 2) with the data from $BaMnO_{2.65}$ being

Table 1
Lattice parameters refined for 4H-$BaMnO_{3-x}$ and 4H-$Ba_{0.5}Sr_{0.5}MnO_{3-x}$ samples

	a (Å)	c (Å)	Volume (Å^2)
$BaMnO_{3-x}$	5.6833(2)	9.3556(4)	261.70(3)
$BaMnO_3$	5.6376(2)	9.2241(3)	253.89(2)
$Ba_{0.5}Sr_{0.5}MnO_{3-x}$	5.58539(8)	9.2123(1)	248.891(8)
$Ba_{0.5}Sr_{0.5}MnO_3$	5.5528(1)	9.1471(2)	244.25(1)

Table 2
Structural parameters refined for 4H-(Ba, Sr)MnO_{3-x} phases in space group $P6_3/mmc$

		$BaMnO_{3-x}$	$BaMnO_3$	$Ba_{0.5}Sr_{0.5}MnO_{3-x}$	$Ba_{0.5}Sr_{0.5}MnO_3$
Ba/Sr(1)	Fraction	1/0	1/0	0.67(1)/0.33(1)	0.68(1)/0.32(1)
	$\mathrm{Uiso}_{\mathrm{equiv}}$	0.00241	0.00112	0.00259	0.00115
Ba/Sr(2)	Fraction	1/0	1/0	0.33(1)/0.67(1)	0.32(1)/0.68(1)
	$\mathrm{Uiso}_{\mathrm{equiv}}$	0.00112	0.00088	0.00146	0.00110
Mn	z	0.60855(9)	0.61274(8)	0.6091(2)	0.6112(2)
	$\mathrm{Uiso}_{\mathrm{equiv}}$	0.0085	0.00081	0.00082	0.00080
O(1)	Fraction	0.971(3)	0.980(2)	1	1
	$\mathrm{Uiso}_{\mathrm{equiv}}$	0.00145	0.00110	0.00191	0.00123
O(2)	x	−0.18961(5)	−0.18715(3)	−0.1861(1)	−0.1839(1)
	y	−0.3792(1)	−0.37429(7)	−0.3722(3)	−0.3679(2)
	Fraction	0.760(2)	0.987(2)	0.852(4)	0.978(5)
	$\mathrm{Uiso}_{\mathrm{equiv}}$	0.00152	0.00107	0.00159	0.00088
wR_p		5.53%	5.83%	4.11%	5.26%
R_p		5.04%	5.04%	3.10%	4.03%
Titration stoichiometry		$BaMnO_{2.65(1)}$	$BaMnO_{3.00(1)}$	$Ba_{0.5}Sr_{0.5}Mn_{2.79(1)}$	$Ba_{0.5}Sr_{0.5}Mn_{2.99(1)}$
Diffraction stoichiometry		$BaMnO_{2.59(1)}$	$BaMnO_{2.95(1)}$	$Ba_{0.5}Sr_{0.5}Mn_{2.77(1)}$	$Ba_{0.5}Sr_{0.5}Mn_{2.96(1)}$

Atomic positions: Ba/Sr(1), $2a$ (0,0,0); Ba/Sr(2), $2c$, ($\frac{1}{3}$, $\frac{2}{3}$, $\frac{1}{4}$); Mn, $4f$, ($\frac{1}{3}$, $\frac{2}{3}$, z); O(1), $6g$, ($\frac{1}{2}$, 0, 0); O(2), $6h$, (x, y, $\frac{1}{4}$).

Table 3
Selected bond lengths (Å) and angles (deg.) extracted from the structures of 4H-(Ba, Sr)MnO_{3-x} phases

	$BaMnO_{3-x}$	$BaMnO_3$	$Ba_{0.5}Sr_{0.5}$ MnO_{3-x}	$Ba_{0.5}Sr_{0.5}$ MnO_3
Ba(1)–O(1)	2.8417(1)	2.8188(1)	2.793(1)	2.776(1)
Ba(1)–O(2)	2.9924(4)	2.9424(2)	2.923(1)	2.891(1)
Ba(2)–O(1)	2.8570(9)	2.82249(9)	2.811(1)	2.793(1)
Ba(2)–O(2)	2.8506(1)	2.8259(1)	2.799(1)	2.781(1)
Mn–O(1)	1.9295(5)	1.9313(4)	1.900(1)	1.898(1)
Mn–O(2)	1.9372(7)	1.9081(6)	1.927(2)	1.917(1)
Mn–Mn	2.647(2)	2.532(2)	2.596(3)	2.539(3)
Mn–O(1)–Mn	180.00(2)	180.00(2)	179.99(5)	179.99(5)
Mn–O(2)–Mn	86.17(4)	83.14(4)	84.69(1)	82.93(1)

asymmetric about the origin, suggesting spin-glass behaviour in this phase.

Neutron powder diffraction data collected from $BaMnO_{2.65}$ at 5 K do not show any features which cannot be accounted for using a simple nuclear scattering model based on the room temperature structure. However, neutron powder diffraction data collected from $BaMnO_{3.00}$ at 5 K show additional diffraction intensity, when compared with the analogous 295 K data set, which was assigned as a magnetic scattering contribution. The simple antiferromagnetic-ordering model reported for $SrMnO_3$ [10,16], with spins aligned parallel to the x-axis, (Fig. 3) was added to the structural model to account for this additional intensity and a good fit was achieved to the diffraction data on refinement (Fig. 4, Table 4). An ordered moment of 2.71(2) μ_B per manganese ion was obtained. The divergence between the zero field-cooled and field-cooled data collected from $BaMnO_{3.00}$ and the associated magnetic hysteresis observed at 5 K suggest the material is in fact a canted antiferromagnet.

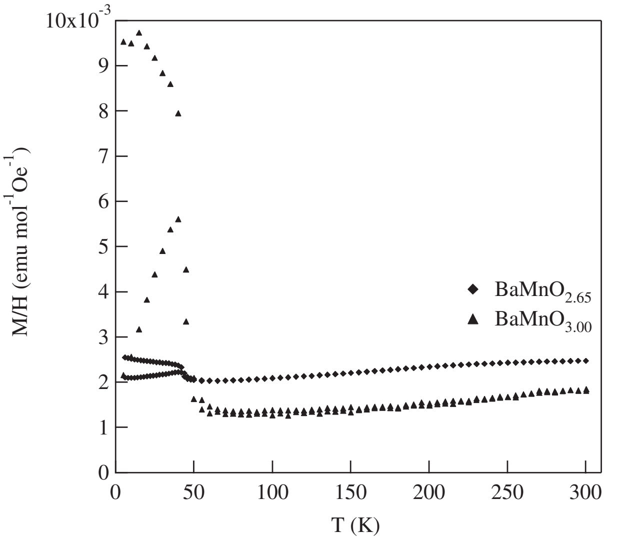

Fig. 1. Zero field-cooled and field-cooled magnetisation data collected from 4H-$BaMnO_{2.65}$ and 4H-$BaMnO_{3.00}$.

The magnetic behaviour of the mixed barium–strontium phases is more complex. Temperature-dependant magnetisation data collected from $Ba_{0.5}Sr_{0.5}MnO_{2.99}$ show the same general form as $BaMnO_{3.00}$; however, the zero field-cooled and field-cooled data diverge at $T\sim265$ K before undergoing a much larger transition at $T\sim50$ K (Fig. 5). Similarly the magnetisation data collected from $Ba_{0.5}Sr_{0.5}MnO_{2.79}$ diverge at $T\sim150$ K prior to the 50 K transition and in contrast to the all-barium phases, the field-cooled magnetisation of $Ba_{0.5}Sr_{0.5}MnO_{2.79}$ is much

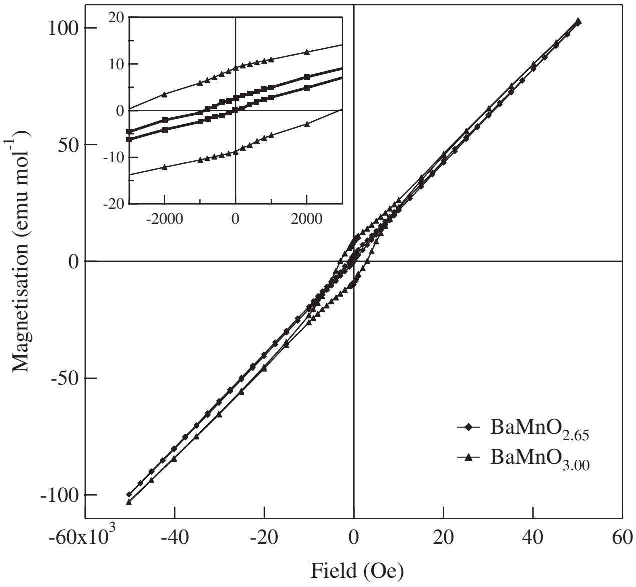

Fig. 2. Magnetisation-field isotherms collected at 5 K from 4H-$BaMnO_{2.65}$ and 4H-$BaMnO_{3.00}$.

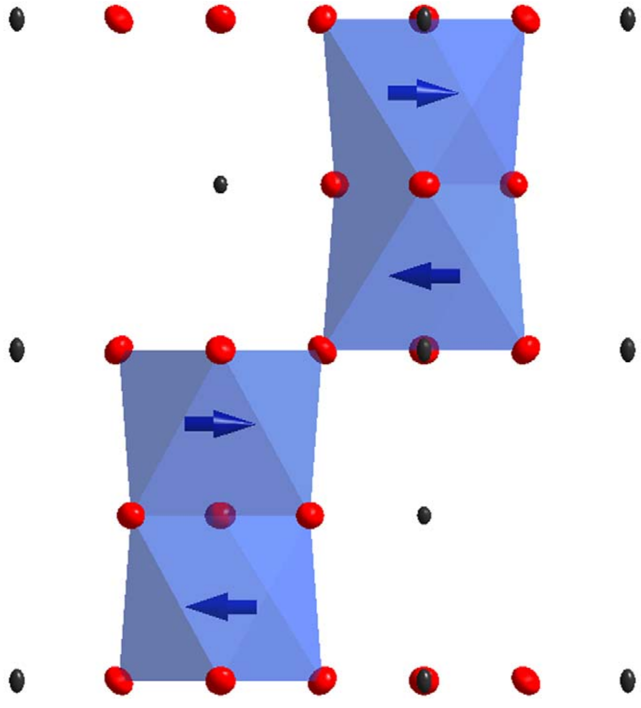

Fig. 3. Representation of the relative spin directions in the antiferromagnetically ordered model obtained from neutron powder diffraction data collected from 4H-$BaMnO_{3.00}$ at 5 K.

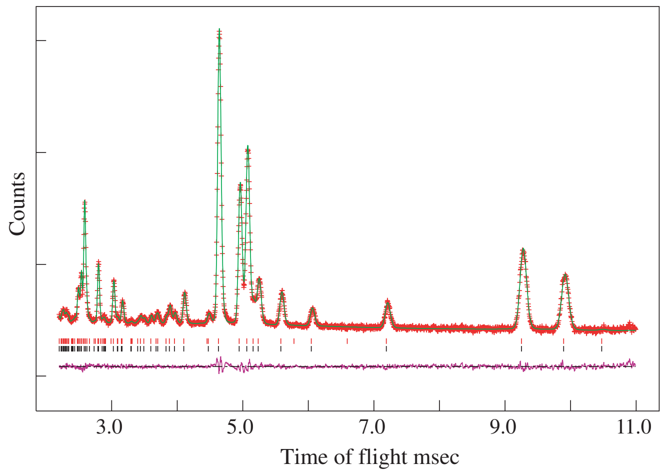

Fig. 4. Observed, calculated and difference plots from the structural refinement of $BaMnO_{3.00}$ against neutron powder diffraction data collected at 5 K. Lower tick marks represent reflection positions for the nuclear model, upper tick marks the magnetic model.

Table 4
Structural and magnetic parameters refined for $(Ba/Sr)MnO_3$ samples from neutron powder diffraction data collected at 5 K

		$BaMnO_3$	$Ba_{0.5}Sr_{0.5}MnO_3$
a (Å)		5.62732(8)	5.5390(1)
c (Å)		9.2080(1)	9.1236(1)
Ba/Sr(1)	Fraction	1/0	0.67(1)/0.33(1)
	$Uiso_{equiv}$	0.0021	0.0059
Ba/Sr(2)	Fraction	1/0	0.33(1)/0.67(1)
	$Uiso_{equiv}$	0.0014	0.0058
Mn	z	0.60855(9)	0.6112(2)
	$Uiso_{equiv}$	0.0019	0.0051
	$M_x\mu_B$	2.71(2)	2.61(2)
O(1)	Fraction	0.982(3)	1
	$Uiso_{equiv}$	0.0037	0.0083
O(2)	x	−0.18677(2)	−0.1839(1)
	y	−0.37353(5)	−0.3678(2)
	Fraction	0.990(2)	0.994(2)
	$Uiso_{equiv}$	0.0034	0.0051
wR_p		1.11%	4.80%
R_p		2.05%	3.60%

Space group: $P6_3/mmc$. Atomic positions: Ba/Sr(1), $2a$ (0,0,0); Ba/Sr(2), $2c$, $(\frac{1}{3}, \frac{2}{3}, \frac{1}{4})$; Mn, $4f$, $(\frac{1}{3}, \frac{2}{3}, z)$; O(1), $6g$, $(\frac{1}{2}, 0, 0)$; O(2), $6h$, $(x, y, \frac{1}{4})$.

larger than the analogous oxidized phase at 5 K. Field-cooled magnetisation-field isotherms collected at 5 K from the mixed barium–strontium phases show magnetic hysteresis, with the data from $Ba_{0.5}Sr_{0.5}MnO_{2.79}$ being asymmetric about the origin (Fig. 6).

Neutron powder diffraction data collected from $Ba_{0.5}Sr_{0.5}MnO_{2.99}$ at 5 K show additional diffraction intensity when compared to the 295 K data set (Fig. 7). These additional features can be readily modelled using the antiferromagnetic ordering scheme described for 4H-$BaMnO_{3.00}$ with a refined moment of 2.61(2) μ_B per manganese (Table 4). Neutron powder diffraction data collected from $Ba_{0.5}Sr_{0.5}MnO_{2.79}$ at 5 K do not show any additional sharp diffraction features when compared to the 295 K data set (Fig. 8). A careful comparison of the low-angle regions of the two diffraction patterns reveals that on cooling a broad feature centred around $2\theta \sim 20°$ forms. This position corresponds to the [002] diffraction reflection and

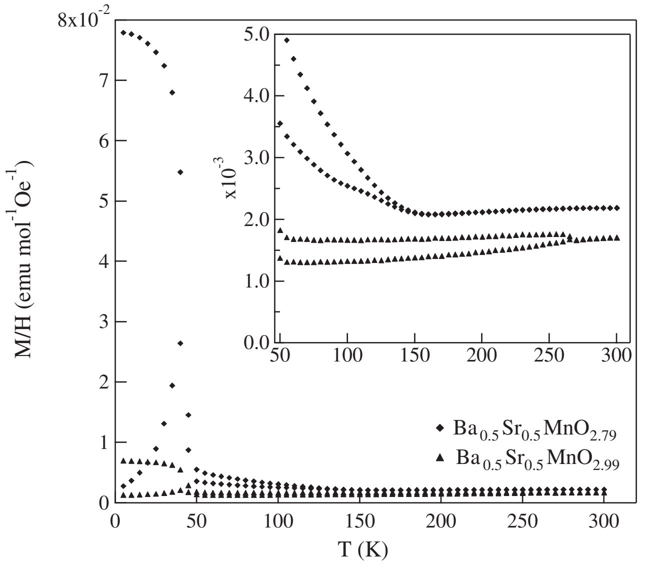

Fig. 5. Zero field-cooled and field-cooled magnetisation data collected from 4H-$Ba_{0.5}Sr_{0.5}MnO_{2.79}$ and 4H-$Ba_{0.5}Sr_{0.5}MnO_{2.99}$. Inset shows the temperature region $50 < T/K < 300$.

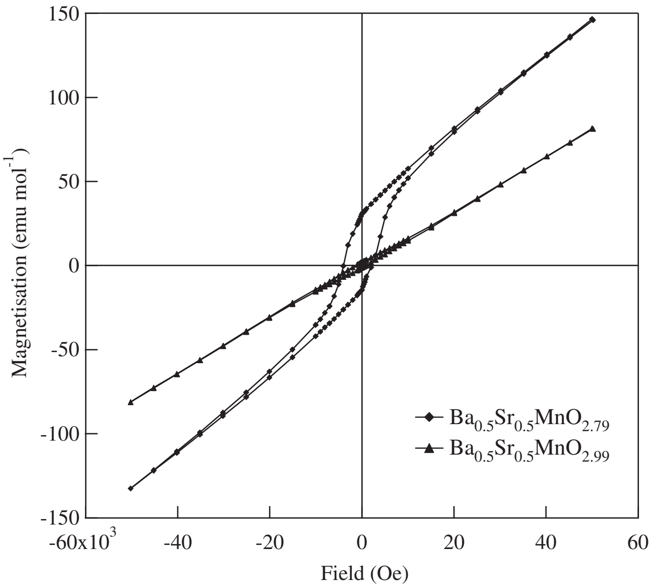

Fig. 6. Magnetisation-field isotherms collected at 5 K from 4H-$Ba_{0.5}Sr_{0.5}MnO_{2.79}$ and 4H-$Ba_{0.5}Sr_{0.5}MnO_{2.99}$.

is interpreted as being due to short-range magnetic ordering with an ordered length too short to yield sharp diffraction reflections.

4. Discussion

The most striking feature of the structures refined for $BaMnO_{2.65}$ and $Ba_{0.5}Sr_{0.5}MnO_{2.79}$ is the localization of the anion vacancies, predominantly in the face-shared sites to form BaO_{3-x} hexagonal layers. This is in agreement with the reported structure of $Ba_{0.5}Sr_{0.5}MnO_{2.84}$ by

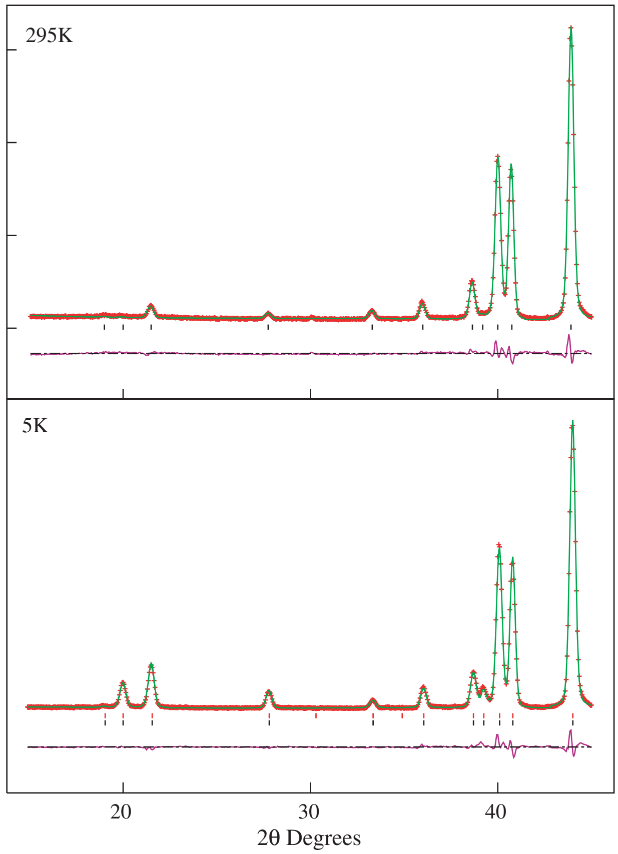

Fig. 7. Observed, calculated and difference plots from the structural refinement of 4H-$Ba_{0.5}Sr_{0.5}MnO_{2.99}$ against neutron powder diffraction data collected at 295 K (upper) and 5 K (lower).

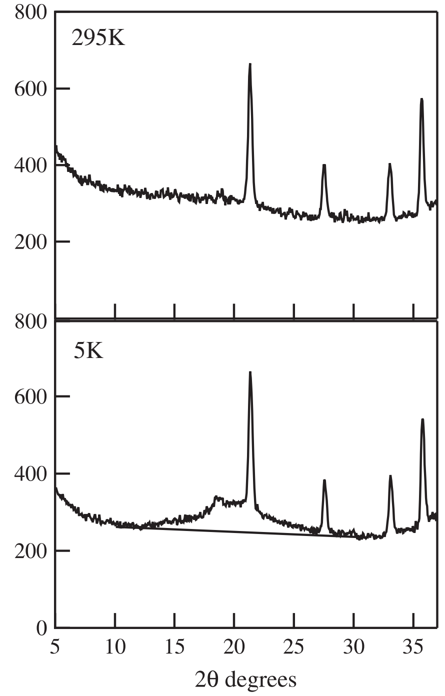

Fig. 8. Comparison of the low-angle portion of neutron powder diffraction data collected from 4H-$Ba_{0.5}Sr_{0.5}MnO_{2.79}$ at 295 K (upper) and 5 K (lower). 5 K data set has a broad feature centred around $2\theta = 20°$.

Jacobson et al. [16]; however, it strongly contradicts the structural model proposed by Gonzalez-Calbet and co-workers for the $BaMnO_{3-x}$ series [17–20]. Gonzalez-Calbet et al. observe that in the series of $BaMnO_{3-x}$ hexagonal phases there is a relationship between the relative proportions of hexagonal and cubic layers and the overall stoichiometry of a phase. This can be expressed by the formula: $x = (0.5c)/(h + c)$, where x is the oxygen non-stoichiometry and c and h are the respective numbers of cubic and hexagonal layers in a repeat unit. This leads them to suggest that the most straight-forward explanation for this relationship is that the oxide ion vacancies are located in the cubic layers giving them an overall formula of $BaO_{2.5}$, which when stacked with the BaO_3 hexagonal layers gives the observed relationship between composition and structure. Our results, and those of the only other neutron diffraction study of a manganese 4H phase [16], unambiguously show this is not the case and that the oxide ion vacancies reside predominantly in the hexagonal layers.

The preferential localization of the oxide ion vacancies within the hexagonal layers can be rationalized by considering the metal–oxygen bonds within the structure (Table 3). Fig. 9 shows the local co-ordination polyhedra of the three metal ion sites of $BaMnO_{2.65}$. It can be seen that there is no significant difference in length between bonds formed by O(1) and O(2) to either the manganese site ($\Delta = 0.007(1)$ Å) or the Ba(2) site ($\Delta = 0.006(1)$ Å). However, O(1) forms a significantly shorter bond than O(2) to Ba(1) ($\Delta = 0.1507(5)$ Å). Thus, locating oxide ion vacancies on the O(2) site removes the longer weaker Ba(1)–O(2) bond rather than the shorter stronger Ba(1)–O(1) bond. This difference in contribution to the total lattice energy of the two oxide ions sites can be highlighted by calculating bond valence sums around each oxide ion [21], which yields the values: $O(1) = +2.135$, $O(2) = +1.968$—the larger value indicating a stronger bonding interaction. Hence, it can be seen that the preference for locating the anion vacancies in the hexagonal layers can be explained on the basis of the lattice energy of the resulting structure and in this instance is mainly driven by the bonding to the Ba(1) site. The changes in lattice constants and bond lengths on oxidation and the substitution of strontium for barium are consistent with the relative ionic radii of Mn(III) and Mn(IV) and Ba(II) and Sr(II).

The low absolute value and weak temperature dependence of the magnetisation of all four samples at $T \sim 300$ K suggests there are strong (antiferromagnetic) interactions between spins in this temperature range. Battle et al. [10] observed similar behaviour for $4H\text{-}SrMnO_3$ and proposed a model in which the super-exchange interactions between manganese centres connected by face sharing of octahedra (Mn–O–Mn∼90°) are much stronger than those connected by apex-sharing (Mn–O–Mn∼180°). This leads to the situation at $T \sim 300$ K where the 90° interactions lead to an antiferromagnetic coupling of spins in the $Mn_2O_{9(-x)}$ dimers, but the 180° interactions are insufficiently strong to bring about full three-dimensional magnetic order. On cooling, full three-dimensional magnetic order does occur in $SrMnO_3$ at $T \sim 278$ K although there is no signature of this in the magnetic susceptibility as the total number of antiferromagnetically paired spins does not change, just their relative orientation. We propose that a similar situation exists in $BaMnO_{3.00}$, and that on cooling, full three-dimensional antiferromagnetic order occurs at

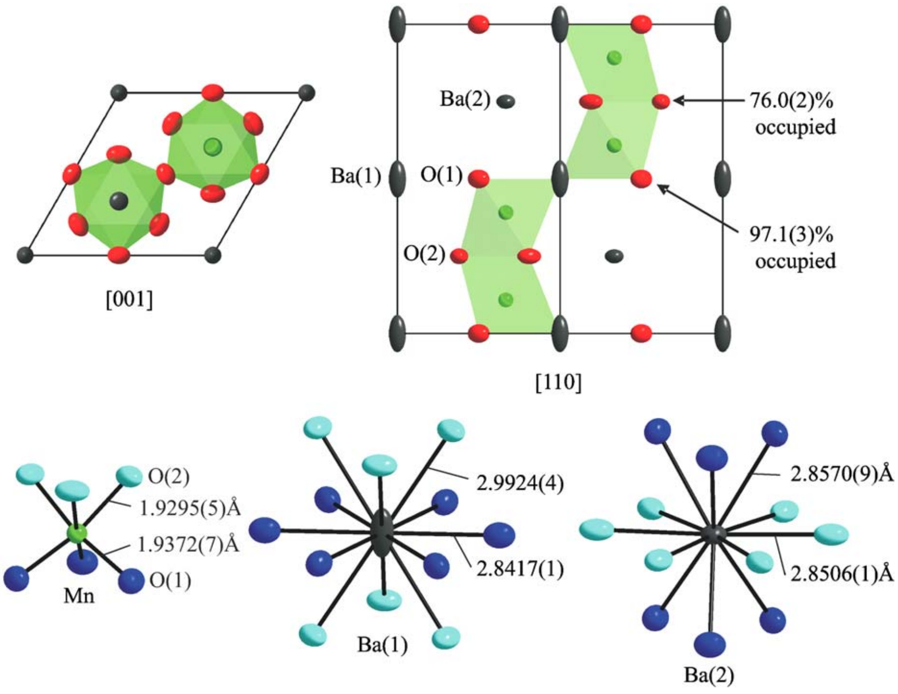

Fig. 9. Representation of the structure of $4H\text{-}BaMnO_{2.65}$ and the local co-ordination polyhedra of the metal cations.

$T > 200$ K. On further cooling, an additional magnetic transition occurs which leads to a canting of the ordered moments at $T \sim 50$ K (Fig. 2). An analogous situation exists for $Ba_{0.5}Sr_{0.5}MnO_{2.99}$, but we propose that the transition observed in the magnetic susceptibility of this phase at $T \sim 260$ K (Fig. 5) corresponds to the onset of full three-dimensional magnetic order. This hypothesis could be confirmed by a complete temperature-dependant neutron powder diffraction study. The lower ordering temperature observed for $Ba_{0.5}Sr_{0.5}MnO_{2.99}$ compared to $SrMnO_3$ can be justified on the basis of a longer Mn–O(1)–Mn bond in the former phase (1.898(1)Å) compared to the later (1.872(5)Å(10)) and thus a correspondingly weaker super-exchange interaction through this bond.

The lack of long-range magnetic order in the anion-deficient phases suggests that Mn(III)/(IV) charge disorder leads to magnetic frustration. This is supported by the observation of spin-glass behaviour at low temperatures in these phases. $Ba_{0.5}Sr_{0.5}MnO_{2.79(1)}$ has an average manganese oxidation state of Mn $+3.58(2)$, very close to a 1:1 mixture of Mn(III) and Mn(IV). The observation of short-range magnetic order in this material allows an interesting comparison with mixed valent cubic perovskite and Ruddlesden–Popper manganates with similar mixed manganese oxidation states. $YSr_2Mn_2O_7$ for instance has a mean manganese oxidation state of $+3.5$ and exhibits similar low angle diffuse scattering in low temperature neutron diffraction data sets which has been assigned as being due to the frustration of magnetic order by a disordered array of Mn(III) and Mn(IV) centres [22].

5. Conclusion

Utilizing high- and low-temperature reaction steps under different oxygen partial pressures, the metastable phases 4H-$BaMnO_3$ and 4H-$Ba_{0.5}Sr_{0.5}MnO_{2.99}$ have been prepared. Neutron powder diffraction data collected at 5 K show that both phases adopt antiferromagnetic ordered structures. Neutron powder diffraction data unambiguously show that the anion vacancies are present in the hexagonal layers of the thermodynamic phases 4H-$BaMnO_{2.65}$ and 4H-$Ba_{0.5}Sr_{0.5}MnO_{2.79}$, contrary to previous structural models, suggesting a further re-examination of other $BaMnO_{3-x}$ phases is required.

Acknowledgments

We thank R. Smith, R.M. Ibberson and E. Suard for assistance collecting neutron powder diffraction data and the Royal Society and the EPSRC for funding this work.

References

[1] K. Chahara, T. Ohno, M. Kasao, Y. Kozono, Appl. Phys. Lett. 63 (1993) 1990.

[2] R. von Helmolt, J. Wecker, B. Holzapfel, L. Schultz, K. Sanwer, Phys. Rev. Lett. 71 (1993) 2331.

[3] P. Schiffer, A.P. Ramirez, W. Bao, S.-W. Cheong, Phys. Rev. Lett. 75 (1995) 3336.

[4] V.M. Goldschmidt, Naturwissenschaften 14 (1926) 477.

[5] C.N.R. Rao, A.K. Cheetham, R. Mahesh, Chem. Mater. 8 (1996) 2421.

[6] B. Raveau, A. Maignan, C. Martin, M. Hervieu, Chem. Mater. 10 (1998) 2641.

[7] D. Dabrowski, O. Chmaissem, J. Mais, S. Kolesnik, J.D. Jorgensen, S. Short, J. Solid State Chem. 170 (2003) 154.

[8] J.B. Goodenough, Magnetism and the Chemical Bond, Wiley, New York, 1963.

[9] K.R. Poeppelmeier, M.E. Leonowicz, J.C. Scanlon, J.M. Longo, W.B. Yelon, J. Solid State Chem. 45 (1982) 71.

[10] P.D. Battle, T.C. Gibb, C.W. Jones, J. Solid State Chem. 74 (1988) 60–66.

[11] E.J. Cussen, P.D. Battle, Chem. Mater. 12 (2000) 831–838.

[12] T. Negas, R.S. Roth, J. Solid State Chem. 3 (1971) 323.

[13] M.A. Hayward, Chem. Commun. (2004) 170.

[14] A.C. Larson, R.B. Von Dreele, General Structural Analysis System, Los Alamos National Laboratory, Los Alamos, 1994.

[15] P.A. Hardy, Acta Crystalogr. 15 (1962) 179.

[16] A.J. Jacobson, A.J.W. Horrox, Acta Crystallogr., Sect. B: Struct. Sci. B 32 (1976) 1003–1008.

[17] J.M. Gonzalez-Calbet, M. Parras, J.M. Alonso, M. Vallet-Regi, J. Solid State Chem. 106 (1993) 99–110.

[18] J.M. Gonzalez-Calbet, M. Parras, J.M. Alonso, M. Vallet-Regi, J. Solid State Chem. 111 (1994) 202–207.

[19] M. Parras, J.M. Alonso, J.M. Gonzalez-Calbet, M. Vallet-Regi, J. Solid State Chem. 117 (1995) 21–29.

[20] M. Parras, J.M. Gonzalez-Calbet, J.M. Alonso, M. Vallet-Regi, J. Solid State Chem. 113 (1994) 78–87.

[21] N.E. Brese, M. O'Keefe, Acta Crystallogr., Sect. B: Struct. Sci. B 47 (1991) 192–197.

[22] P.D. Battle, J.E. Millburn, M.J. Rosseinsky, L.E. Spring, J.F. Vente, Chem. Mater. 9 (1997) 3136.